A novel temperature calculation method of canned permanent magnet synchronous motor for vacuum pump

MING LI ⬛✉, SHUXIAN LUN, HAIQI MU, WEI WANG

School of Control Science and Engineering, Bohai University
No.19, Keji Road, Jinzhou, People's Republic of China
e-mail: ✉ *lmpmsm@163.com, lunshuxian@qymail.bhu.edu.cn*

Abstract: Accurate temperature prediction is vital for the canned permanent magnet synchronous motor (CPMSM) used in the vacuum pump, as it experiences severe heating. In this paper, a novel motor temperature calculation method is proposed, which takes into account the temperature impact on the heat transfer capacity. In contrast to existing electromagnetic-thermal coupled calculation methods, which solely address the temperature effect on the motor electromagnetic field, the proposed method comprehensively considers its impact on motor losses, permanent magnet magnetic properties, thermal conductivity, and heat dissipation ability of motor components, resulting in a motor temperature simulation that closely resembles the actual physical process. To verify the reliability of the proposed temperature calculation method, a 1.5 kW CPMSM was chosen as the research subject. The method was used to analyze the temperature distribution characteristics of the motor and assess the impact of ambient temperature on motor temperature rise. Furthermore, a prototype was fabricated, and an experimental platform was established to test the motor temperature. The results demonstrate good agreement between the calculated results obtained using the proposed method and the experimental data. This research not only provides a theoretical foundation for optimizing the design of the CPMSM but also provides valuable insights into its operational safety and reliability.

Key words: canned PMSM, heat-transfer capacity, temperature, vacuum pump

1. Introduction

Vacuum pumps are extensively applied in fields such as chemical engineering, integrated circuit manufacturing, and the nuclear industry due to their advantages of safety, high efficiency, and leakage-free operation [1]. To improve the efficiency of the vacuum pump, canned permanent magnet synchronous motors (CPMSMs) are commonly used for driving vacuum pumps [2]. Compared with conventional PMSMs, CPMSMs require the installation of a can sleeve inside the stator to prevent vacuum leakage. The can sleeve is closely attached to the inner surface of the stator, resulting in additional eddy current losses under the action of the rotating magnetic field in the air gap, thereby leading to an increase in motor temperature [3]. Additionally, the rotor of the CPMSM used in vacuum pumps operates in a vacuum environment, and the heat transfer relies solely on radiation for cooling. The inferior heat dissipation conditions for the rotor make it more susceptible to overheating compared to conventional permanent magnet synchronous motors (PMSMs), possibly leading to irreversible demagnetization of the permanent magnets [4]. Therefore, accurately calculating the temperature of the CPMSM used in vacuum pumps is of practical significance in improving the prediction accuracy of the motor electromagnetic performance and ensuring its safe and reliable operation.

Extensive researches have been conducted on the temperature calculation of the canned motor [5–9]. Currently, the calculation methods for motor temperature mainly include the thermal circuit method, equivalent thermal network method, and finite element method. However, the thermal circuit method can only estimate the average temperature of windings and stator cores, and cannot fully characterize the temperature distribution and the location and values of hotspots. Therefore, the temperature field of canned motors used in vacuum pumps is mostly analyzed using the equivalent thermal network method and the finite element method. In [10], an equivalent thermal network program was developed for the rapid analysis of the steady-state temperature of the canned switched reluctance motor. However, the specific process of heat transfer between the stator, rotor can, and the air gap was not provided. Yu Q. *et al.* proposed a lumped parameter thermal network model with compensation components to calculate the temperature of the CPMSM, which has the advantages of requiring fewer computational resources and a fast calculation speed [11]. Although the equivalent thermal network method has lower hardware resource requirements, its calculation accuracy is slightly lower than that of the finite element method. An Y. *et al.* investigated the temperature field of a single-phase canned induction motor (CIM) used in vacuum pumps using three-dimensional finite element method. By comparing it with experimental data, it is found that the finite element method exhibits a high accuracy [12]. In [13], a three-dimensional finite element model with electromagnetic-thermal unidirectional coupling was established for a vacuum pump switch reluctance motor, and this model was used to analyze the motor temperature field. The analysis results revealed that the rotor of the switch reluctance motor experiences the most severe heating among all the components. In [14], a fluid-solid unidirectional coupling method was employed to analyze the temperature of a CIM used in a nuclear pump, and the flow velocity distribution and the motor temperature distribution were computed. To further enhance the accuracy of the motor temperature calculation, Li Y proposed using an electromagnetic-thermal bidirectional coupling method to compute the temperature of an 8 kW PMSM used in traction, and the distribution law of motor temperature field was obtained [15].

The CPMSM exhibits a bidirectional coupling relationship between its temperature field, electromagnetic field, and fluid field. Temperature influences both the electromagnetic field through changes in material electromagnetic properties and the temperature distribution by altering the material thermal parameters. However, to the best of the author knowledge, there is currently no temperature calculation method that considers the temperature influence on the motor heat transfer capability. Therefore, this paper proposes a motor temperature calculation method that considers the temperature impact on heat transfer capability to enhance the accuracy of temperature calculation for the CPMSM. The proposed method enables a comprehensive simulation of the actual motor heat dissipation process, significantly enhancing motor temperature prediction accuracy, and ensuring safe and reliable motor operation.

The structure of this paper is organized as follows: the proposed temperature calculation method is introduced in Section 2. The proposed method is applied in Section 3 to compute the motor temperature and analyze the influence of ambient temperature on the motor temperature rise. The proposed temperature calculation method is validated through experiments in Section 4, and the conclusion is presented in Section 5.

2. Motor temperature calculation method considering the influence of temperature on heat-transfer capacity

2.1. The temperature calculation process

The calculation process of the proposed method is illustrated in Fig. 1.

In Fig. 1, the temperature solution process involves the following steps:

1. Set the initial temperature, typically the ambient temperature, as the temperature for all components of the motor.
2. Determine material properties, thermal characteristics, and fluid medium parameters based on the initial temperature, and separately calculate the electromagnetic and fluid fields.
3. Transfer the calculated losses (copper loss, core loss, can loss, and rotor eddy current loss) and heat dissipation conditions into the temperature model to compute the motor temperature distribution.
4. The iteration converges; when the temperature differences between the results obtained in this iteration and the results obtained in the last iteration of the permanent magnet, winding, can sleeve, and fluid temperatures are less than ε, the iteration is defined to be convergent. If not, update the component temperatures in the electromagnetic, fluid, and temperature fields, and reiterate the losses and motor output characteristics calculation in the electromagnetic field until the temperature differences are smaller than ε. ε is a threshold value set for judging iterative convergence.

The smaller the threshold ε is, the higher the calculation accuracy is, but the iteration time increases accordingly. According to the IEC60034-2, if the temperature difference between the front and rear of the motor does not exceed 1°C within one hour after operating under its specified conditions for a certain period of time, it indicates that the temperature of the motor has stabilized. Therefore, the threshold ε is determined as 1°C in this study. We have supplemented this information about ε in the revised manuscript based on your feedback.
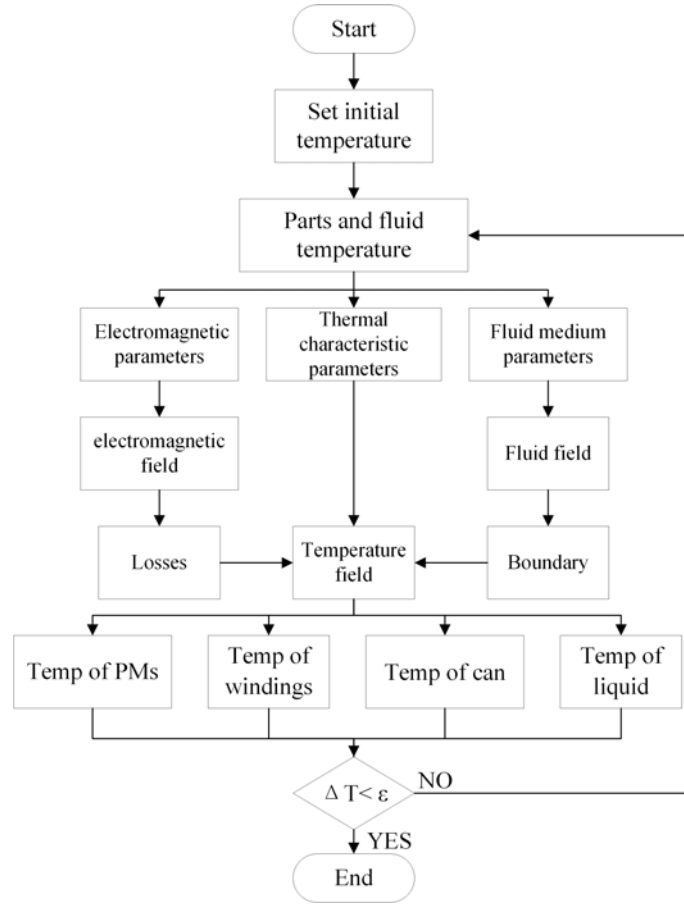
Fig. 1. Solution process for proposed temperature calculation method

2.2. The temperature calculation process

The losses of a CPMSM include copper loss, core loss, can loss, rotor eddy current loss, and mechanical loss, where mechanical loss is obtained empirically [16]. Therefore, this section mainly introduces the calculation methods of other losses.

The copper loss of stator winding mainly refers to the loss generated by the working current in the winding resistance, which can be calculated according to Eq. (1) [17].

$$
\begin{cases}
p_{cu} = mI^2 R_{AC} \\
R_{AC} = k_{1R} R_{DC} \quad , \\
R_{DC} = \rho l / A
\end{cases}
\tag{1}
$$

where: m is the phase number, I is the phase current, R_{AC} is AC resistance considering the proximity effect, k_{1R} is the proximity effect coefficient for the armature resistance, R_{DC} is DC resistance, l is the axial length of the winding, A is the cross-sectional area of the conductor, ρ is the electrical resistivity of the winding.

The electrical conductivity of copper is $\rho_{15} = 0.0175 \times 10^{-6}$ Ω·m at a temperature of 15°. The resistivity is related to the temperature, and within the normal operating temperature range of the motor, and the relationship between temperature and resistance is shown in Eq. (2) [18].

$$\rho_i = \rho_{15} \left[1 + \alpha \left(T - T_{15} \right) \right], \tag{2}$$

where α is the temperature coefficient of resistance, for the copper, $\alpha \approx 0.004°C^{-1}$.

Equations (1) and (2) consider the influence of temperature on the resistance of the stator winding. In the process of temperature calculation, the resistance used for stator copper loss in each iteration is determined by Eqs. (1) and (2), as well as the temperature obtained in the last iteration.

The calculation of core loss is based on the Bertotti loss model, which can be divided into three parts: hysteresis loss, eddy current loss, and excess loss. However, as the excess loss is negligible due to its small contribution, the equation for calculating core losses is [19]:

$$p_{\text{Fe}} = p_h + p_e = k_h f B_m^{\alpha_m} + k_e f^2 B_m^2, \tag{3}$$

where: p_h, p_e are hysteresis loss and eddy current loss, respectively, and B_m is the magnetic flux density of the core. k_h is a material dependent constant, and k_e is also a material dependent constant that is proportional to the square of the material thickness. In addition, k_h and k_e involve the increase in losses due to metallurgical and manufacturing processes. In general, k_h and k_e are determined by manufacturer's experiments and provided to consumers.

The flux density of the CPMSM is mainly produced by permanent magnets. At present, the permanent magnets are mainly Nd–Fe–B. The disadvantages of Nd–Fe–B are low Curie temperature, generally about 310 ~ 410°, and high temperature coefficient, with the temperature coefficient of the remanence B_r is –0.13% K^{-1} and the coercivity H_c is $-0.6 \sim -0.7\%$ K^{-1} [20].

The calculation equation for the remanence considering temperature influence is [21]:

$$B_r = \left[1 + (T - 20) \frac{\alpha_{Br}}{100} \right] \left(1 - \frac{IL}{100} \right) B_{r20}, \tag{4}$$

where: T is the operating temperature of the permanent magnets, α_{Br} is the temperature coefficient of the B_r, B_{r20} is the remanence of permanent magnets under the ambient temperature 20°, IL is irreversible loss of magnetic properties of permanent magnets. Due to the fact that the temperature of permanent magnets did not reach the Curie temperature in this study, it is assumed that the permanent magnet did not undergo irreversible demagnetization.

The calculation equation for the coercivity considering temperature influence is [21]:

$$H_c = \left[1 + (T - 20) \frac{\alpha_{Hc}}{100} \right] \left(1 - \frac{IL}{100} \right) H_{c20}, \tag{5}$$

where: α_{Hc} is the temperature coefficient of the H_c, H_{c20} is the coercivity of permanent magnets under the ambient temperature 20°.

In the iterative calculation of temperature, the magnetic properties of the permanent magnets and the core loss used in temperature calculation are determined by Eqs. (3)–(5) and the temperature obtained in the last iteration, respectively.

In addition, the computation of can loss and rotor eddy current loss requires considering not only the temperature influence on the remanence and coercivity of the permanent magnets but also its effect on the material conductivity, which influences the eddy current losses.

2.3. Thermal conductivity and dissipation coefficient considering temperature influence

The motor operates as a heat transfer system with an internal heat source, primarily involving heat conduction and convection processes. According to the fundamental principles of heat transfer, this process depends directly on the medium thermal conductivity and dissipation coefficient. Therefore, when calculating the motor steady-state temperature, the focus lies on studying the thermal conductivity and dissipation coefficient within the motor.

The thermal conductivity is affected by the material properties, and it varies with factors such as temperature, pressure, humidity, porosity, and uniformity for a given material. Temperature usually plays a decisive role, and the thermal conductivity can be roughly approximated to change linearly [22].

$$\lambda = \lambda_0 \left(1 + bT_a\right), \tag{6}$$

where: λ_0 is the thermal conductivity at $0°$, b is the temperature coefficient, and T_a is the actual temperature of the material.

Based on [22], the temperature coefficient of thermal conductivity of silicon steel sheet is $3 \times 10^{-2}\,°\mathrm{C}^{-1}$, that of winding copper is $-0.2 \times 10^{-2}\,°\mathrm{C}^{-1}$, that of steel is $-4 \times 10^{-2}\,°\mathrm{C}^{-1}$, and that of insulation material is $0.16 \sim 0.3 \times 10^{-2}\,°\mathrm{C}^{-1}$. The heat transfer coefficient of the housing surface can be calculated according to the following Eq. (7) [23].

$$\gamma = 14 \left(1 + 0.5\sqrt{\omega}_1\right) \sqrt[3]{\left(\frac{\theta}{25}\right)}, \tag{7}$$

where: γ is the heat transfer coefficient of the housing surface, ω_1 is the wind speed on the inner wall of the housing, and θ is the outer surface temperature of the housing.

Equation (8) can be used for calculating the heat transfer coefficient for water cooling mode [23, 24].

$$\gamma_w = 91.8\omega^{1.8} \left(39.5 + \theta^{0.35}\right) d^{-0.2}, \tag{8}$$

where d is the diameter of the cooling channel.

Equations (6)–(8) relate to the influence of temperature on the thermal conductivity of materials, the heat convection coefficients of the housing surface and the cooling channel, respectively. In the iterative calculation of temperature, these heat transfer conditions are determined by Eqs. (6)–(8) and the temperature obtained in the last iteration.

3. Calculation model and conditions of temperature field

3.1. Calculation model of electromagnetic field and temperature field

In this study, a 1.5 kW CPMSM is taken as the research object, and its loss and temperature field are analyzed by using the proposed method. The basic parameters of the motor are shown in Table 1.

To validate the correctness and accuracy of the proposed method, a two-dimensional finite element model is established according to the parameters in Table 1, as shown in Fig. 2.

Figure 2 also includes the mesh results of the finite element model, the distribution of magnetic lines and flux density under the no-load operating conditions of the motor. As can be seen from

Table 1. The parameters of the CPMSM

Parameters	Value
Rated power (kW)	1.5
Phase number	3
Pole number	6
Rated frequency (Hz)	400
Can thickness (mm)	0.5
Winding connection type	Y
Stator slots	9
Polar arc coefficient	0.97
Thickness of PM (mm)	2.5
Stator length (mm)	23
Stator outside diameter (mm)	107
Rotor outside diameter (mm)	46
Grade of the permanent magnet	N38UH
Stator/rotor core material	DW465-50

Fig. 2, the stator of the motor adopts assembled structure, which is beneficial to improve the slot fill factor and the motor efficiency. The rotor adopts surface-mounted magnetic pole structure, which is easy to optimize and improve the performance of the motor. In addition, a temperature
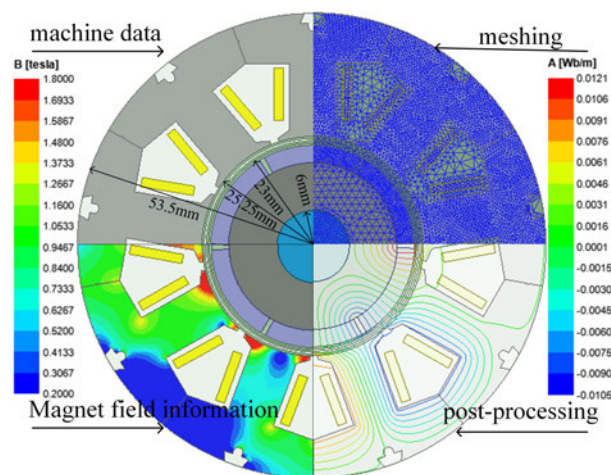
Fig. 2. FEA model of the 1.5 kW CPMSM

calculation model for the CPMSM was developed and illustrated in Fig. 3. The temperature calculation model includes stator windings, stator core, winding insulation, slot wedges, can sleeve, permanent magnets, rotor core, and housing.
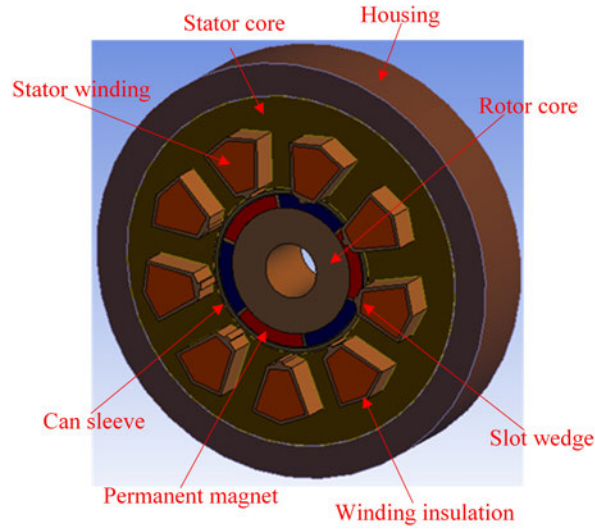

Fig. 3. Temperature field calculation model

3.2. Boundary conditions

The CPMSM incorporates a helical waterway structure to achieve advantages such as uniform motor temperature distribution, minimal inlet-outlet pressure difference, and a straightforward manufacturing process.

The fluid-structure coupling method is utilized in this study to simulate the fluid flow within the motor cooling channel. By adopting this approach, it becomes possible to obtain the heat transfer coefficient within the fluid domain and directly relate it to the temperature calculation model. Consequently, this method effectively solves the challenge of determining the heat transfer coefficient at the interface between the fluid and solid materials.

In fluid calculations, the first assumption is that the cooling liquid enters the cooling waterway perpendicular to the housing. The second assumption is that the cooling liquid carries away all the losses generated by the motor. This is because the thermal balance of a motor is a dynamic process, where the heat generated by the motor is equal to the heat dissipated at any moment when the motor reaches thermal steady-state. The heat dissipation form of the motor includes convective heat dissipation from the cooling channel, natural heat dissipation from the housing, and thermal radiation, but the heat dissipation from natural heat dissipation and thermal radiation is limited compared to the heat dissipation from the cooling channel, so this assumption is made. Therefore, allowing for the determination of the flow velocity of the cooling liquid.

$$P_{\text{loss}} = G c_P \left(T_{\text{out}} - T_{\text{in}} \right), \tag{9}$$

where: G is the flow rate, T_{out} is the outlet temperature, T_{in} is the inlet temperature and c_P is the specific heat capacity.

The function of Eq. (9) is to determine the flow rate of coolant in the cooling channel based on the above assumed conditions.

Assuming that the temperature difference between the inlet and outlet is 5 K, the specific heat capacity of water is 4.2×10^3 J/(kg·K), and the calculated $G = 0.214$ kg/s, the available flow velocity μ is 2.5 m/s.

The helical waterway entrance is assigned as the velocity inlet boundary condition when calculating the fluid field of the CPMSM, with the velocity of 2.5 m/s. The helical waterway outlet is set as the pressure boundary condition with a pressure equivalent to standard atmospheric pressure as cooling liquid is incompressible, and the ambient temperature is set to 25°C.

The fluid field of the cooling liquid inside the motor waterway can be calculated by the finite element method based on the given assumptions and boundary conditions. Figure 4(a) displays the velocity distribution of the cooling liquid in the helical waterway, while Fig. 4(b) illustrates the pressure distribution of the cooling liquid in the same waterway.

According to Fig. 4(a), the maximum velocity of the cooling liquid inside the waterway is 2.757 m/s, the minimum velocity is 2.208 m/s, and the average flow velocity is 2.483 m/s. The uniform cooling liquid flow is conducive to a uniform distribution of motor temperature. Figure 4(b) shows that the inlet-outlet pressure difference in the waterway is 21 200 Pa, and there is no significant occurrence of pressure non-uniformity inside the waterway, resulting in low pressure loss.
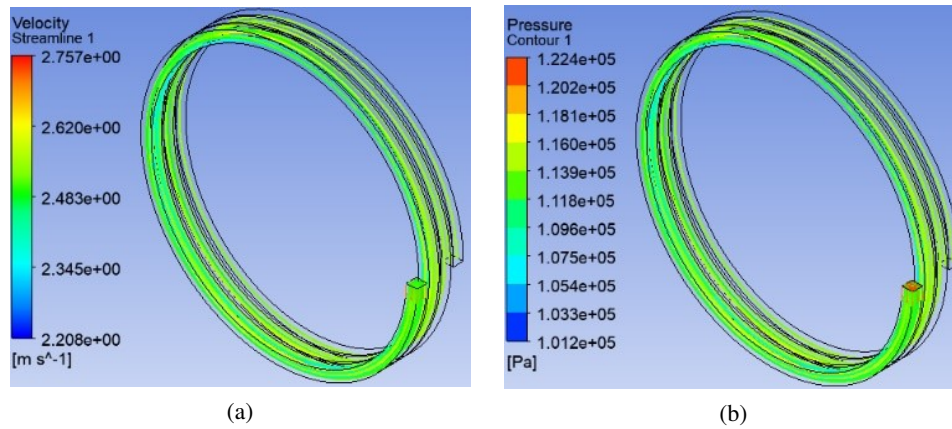

Fig. 4. Distribution of flow velocity and pressure in waterway: velocity distribution (a); pressure distribution (b)

By correlating the above results to the temperature calculation model, the convective heat dissipation coefficient of the waterway can be obtained, and the result is shown in Fig. 5.

As can be seen from Fig. 5, the maximum of heat dissipation coefficient in the waterway is 13 414.9 (W/m²°C), and the maximum appears in the middle of the waterway rather than at the inlet, while the minimum of heat dissipation coefficient is located at the outlet of the waterway.
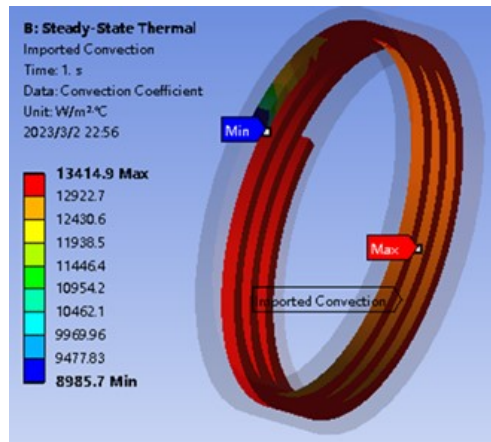
Fig. 5. Convective heat dissipation coefficient in waterways

3.3. The calculation results and analysis

The temperature of the CPMSM is calculated using the method proposed in this paper, based on the losses and the boundary conditions obtained from the finite element model. The temperature distribution of various components in the CPMSM under rated conditions is shown in Fig. 6.
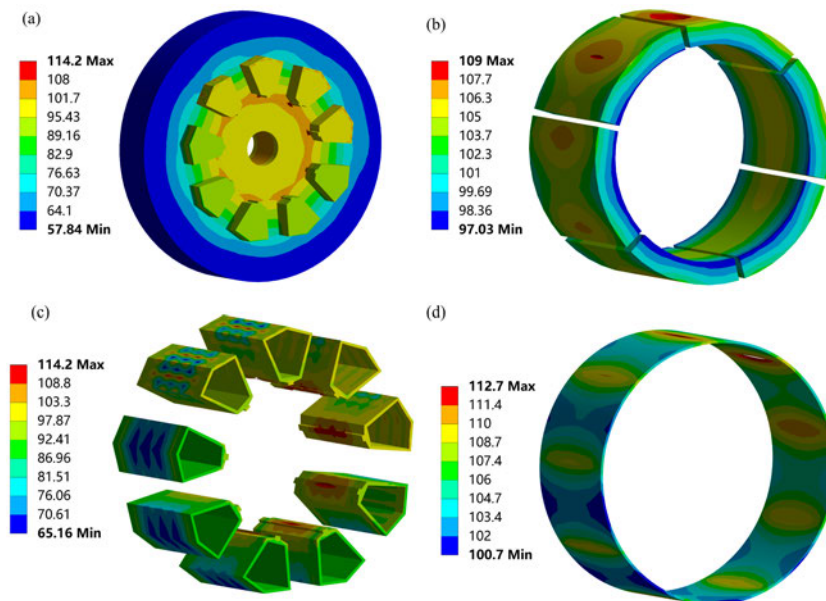

Fig. 6. Temperature distribution of the CPMSM under the rated operating condition: ensemble (a); permanent magnet (b); insulation (c); can sleeve (d)

The maximum temperature of the CPMSM under rated conditions is 114.2°C, as shown in Fig. 6(a) and Fig. 6(c), and the maximum location is found at the winding insulation. The CPMSM is equipped with H-class insulation, which permits a maximum temperature of 180°C, ensuring the safety of the winding insulation during motor operation. Additionally, Fig. 6(b) indicates that the maximum temperature of the permanent magnets is 109°C. The CPMSM uses Nd-Fe-B magnets with a grade of N38UH, which have a Curie temperature of 180°C, providing a significant margin to ensure the safe and reliable operation. Furthermore, Fig. 6(d) reveals that the temperature of the can sleeve is relatively high, reaching a minimum temperature of 100.7°C.

Figure 7 presents the temperature calculation results obtained using electromagnetic-thermal unidirectional coupling, electromagnetic-thermal bidirectional coupling, and the method proposed in this paper, and compares these results.
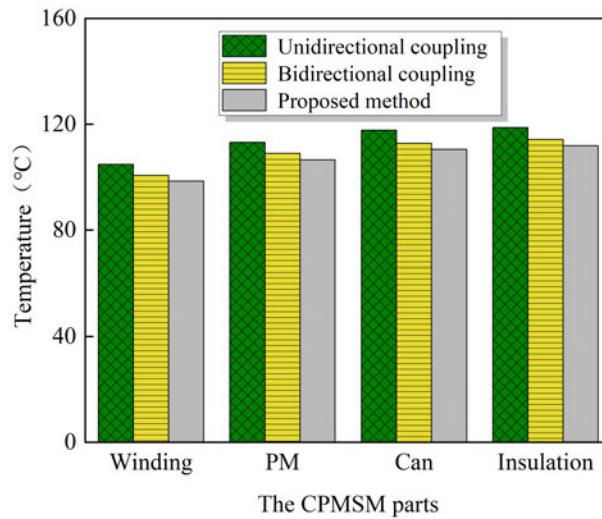

Fig. 7. Comparison of temperature calculation results using different methods

The results from Fig. 7 indicate that the calculations using electromagnetic-thermal unidirectional coupling are higher than those using electromagnetic-thermal bidirectional coupling. This is because unidirectional coupling neglects the impact of temperature on the resistivity of the windings and can sleeve, as well as the magnetic properties of the permanent magnets. When using electromagnetic-thermal bidirectional coupling, although the temperature leads to increased copper loss, it also decreases core loss and can loss, resulting in an overall reduction in motor losses. As a result, the temperature calculation results with electromagnetic-thermal bidirectional coupling are lower than those with electromagnetic-thermal unidirectional coupling. In addition, the results obtained using the proposed method in this paper are lower than those obtained using electromagnetic-thermal bidirectional coupling. This is because the proposed method considers not only the temperature impact on the electromagnetic properties of the material but also its effect on thermal properties. Considering the temperature impact on the material thermal properties enhances the motor material thermal conductivity and heat dissipation capability.

The results obtained using the proposed method show differences of 2.19% in winding temperature, 2.21% in permanent magnet temperature, 1.95% in can temperature, and 2.10% in insulation temperature when compared with the results obtained using electromagnetic-thermal bidirectional coupling.

3.4. Influence of ambient temperature on motor temperature rise

The vacuum pump-driven motor operates in an environment with a wide range of temperature variations. When the ambient temperature changes, the electromagnetic field, temperature field, and fluid field inside the motor also change. The coupling between them becomes more severe, which poses challenges for the study of motor design and the variation patterns of motor characteristics. Therefore, it is necessary to study the temperature of the CPMSM under different ambient temperatures.

The method proposed in this paper was used to calculate the steady-state temperature rise of the stator winding, can sleeve, insulation, and permanent magnets of the motor under various ambient temperatures at rated operating condition. The results are shown in Table 2.

Table 2. Influence of ambient temperature on temperature rise of the motor

T-ambient	TR-winding	TR-PM	TR-can	TR-insulation
–30°C	77.3 K	88.4 K	92.1 K	93.8 K
0°C	75.8 K	86.7 K	90.5 K	91.9 K
30°C	74.1 K	85.2 K	88.9 K	90.2 K

T – Temperature, TR – Temperature rise

It can be seen from Table 2 that when the ambient temperature is –30°C, the steady-state temperature rise of the stator winding, insulation, permanent magnets, and can sleeve is higher than the situation when the ambient temperature is 30°C. This is because when the ambient temperature is –30°C, the core loss, can loss, and rotor eddy current loss are larger than those when the ambient temperature is 30°C. Additionally, the heat conduction and heat dissipation capabilities of the motor materials are better at 30°C than at –30°C, which results in a slightly higher temperature rise when the ambient temperature is –30°C compared to the situation at 30°C. The differences should be considered in the motor design process, which can reduce the requirements for the insulation materials.

4. Experimental verification

4.1. Experimental platform

To verify the results of this paper, a prototype was manufactured and an experimental platform was built, as shown in Fig. 8 and Fig. 9, respectively.

In Fig. 9, the experimental platform consists of the prototype, inverter, torque-speed tester, dynamometer and its controller, cooling equipment and its controller, adjustable temperature

chamber, and various measurement devices such as power analyzer, oscilloscope, temperature monitor, and thermal imaging camera. The prototype inverter utilized is the Kewo AD800N. The power analyzer employed is Fluke NORMA5000, and the oscilloscope selected is Yokogawa DL750.
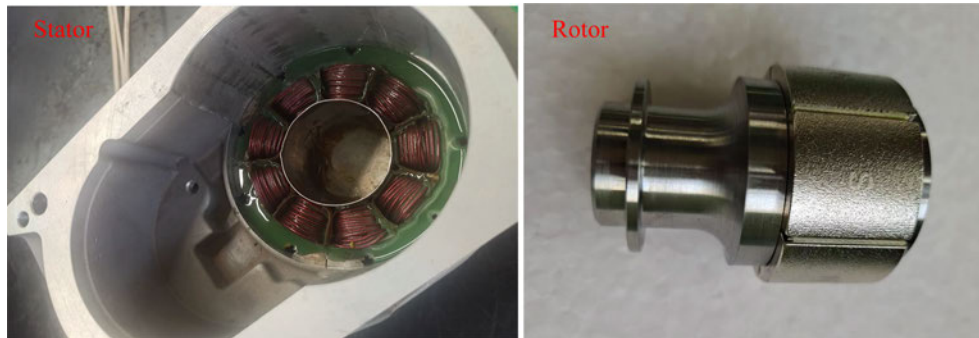

Fig. 8. The prototype

Fig. 9. The experimental platform of the prototype

Figure 10 shows the inside of the adjustable temperature chamber depicted in Fig. 9.

In Fig. 10, the adjustable temperature chamber is used to alter the ambient temperature of the prototype, with a temperature control range of –50°C to 50°C. From Fig. 10, it can be observed that the prototype is connected to the dynamometer through a coupling. Additionally, the temperature monitor and inverter are also placed inside the adjustable temperature chamber.
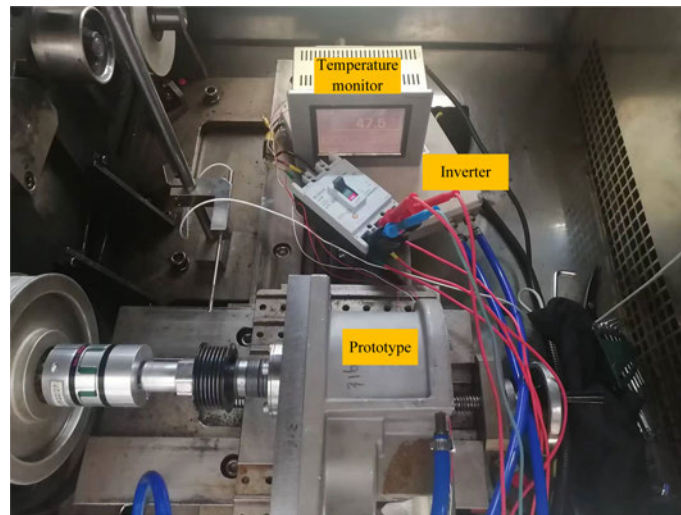
Fig. 10. The adjustable temperature chamber

4.2. Temperature rise test results

The winding insulation temperature of the prototype is measured by a thermocouple embedded inside the winding. The type of the thermocouple is YY-SF-B8-PT100, its temperature measurement range is −200°C–200°C, and its measurement accuracy is 0.1°C. The motor stator with the thermocouple is shown in Fig. 11.
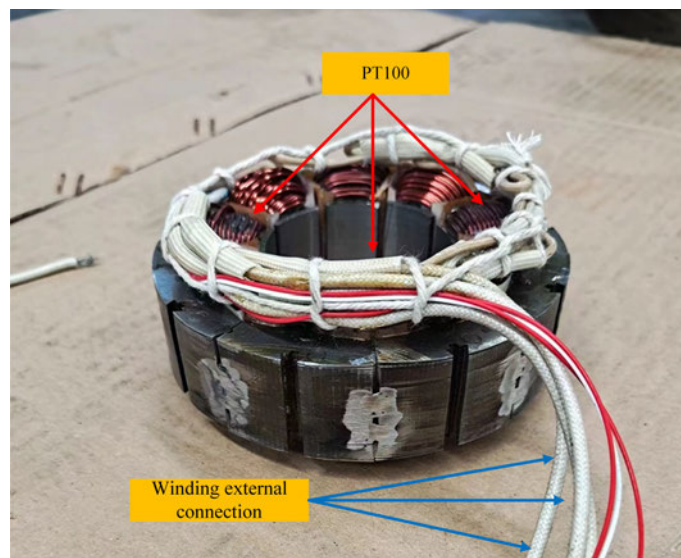

Fig. 11. The stator with the thermocouple

The prototype undergoes temperature measurements under rated load. The cooling liquid flow rate is set to 1.7 m³/h, and the inlet liquid temperature is set at 20°C. The tested motor is subjected to thermal testing at temperature chamber settings of –30°C, 0°C, and 30°C, respectively.

Figure 12 shows the variation curves of the winding insulation temperature of the prototype under three ambient temperature conditions.
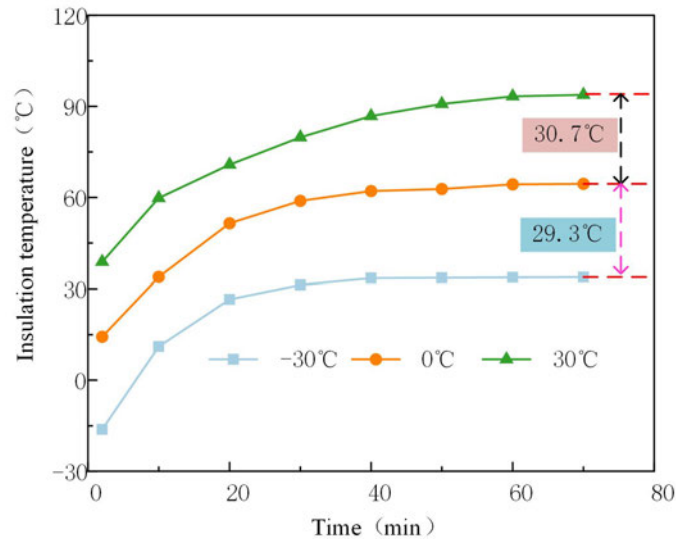

Fig. 12. The winding insulation temperature of the prototype

It can be observed from Fig. 12 that the variation of the insulation temperature is similar under different ambient temperature conditions, but the temperature rise of the motor is different under different environmental temperatures. Within 20 minutes, the rate of temperature rise is higher. With further increase in time, the rate of the insulation temperature rise slows down, and after 70 minutes, the insulation temperature stabilizes. Furthermore, it can be observed from Fig. 12 that the lowest insulation temperature occurs at an ambient temperature of –30°C, followed by 0°C, and the highest insulation temperature occurs at 30°C, reaching approximately 100°C. Compared to the maximum temperature limit of Class F insulation, it still has a significant temperature margin.

By subtracting the ambient temperature from the steady-state temperature of the winding insulation, the steady-state temperature rise of the CPMSM under three ambient temperature conditions can be obtained, as presented in Table 3. Table 3 also provides the corresponding calculation results of the winding insulation temperature rise to compare.

Table 3 indicates that the steady-state temperature rise of the winding insulation does not differ significantly under three ambient temperature conditions. This may be because although the increase in ambient temperature enhances the heat transfer capability, it also deteriorates the electromagnetic performance of the motor, leading to the heat sources increase. Furthermore, Table 3 shows that there is good consistency between the calculated and measured values of the winding insulation temperature rise, with a temperature rise error of approximately 5% under three ambient temperature conditions.

Table 3. The temperature rise of winding insulation under different ambient

Ambient temperature	Test results	Calculated results	Error (%)
–30°C	66.8 K	63.4 K	5.1
0°C	64.5 K	61.2 K	5.1
30°C	63.8 K	60.7 K	4.9

5. Conclusions

This paper investigates the relationship between temperature and the physical properties of motor materials, including thermal parameters, and heat dissipation coefficients. It reveals the temperature variation characteristics of the CPMSM used in vacuum pumps when considering the temperature influence. The analysis also examines the impact of ambient temperature on the motor temperature distribution. The obtained conclusions are as follows:

1. A temperature calculation method is proposed that takes into account the mutual iteration of multiple physical fields considering temperature effects. This method not only considers the impact of temperature on motor electromagnetic performance but also incorporates its influence on motor heat transfer capacity. The research results show that this method can more closely simulate the actual multi-physical field processes and effectively improve the accuracy of temperature calculation for CPMSMs.

2. The convective heat transfer coefficient of the motor cooling channel was determined through fluid-structure coupling calculation. Due to the influence of the cooling channel structure and internal flow resistance, the maximum of the convective heat transfer coefficient inside the cooling channel is not at the inlet, and the value is 1.34×10^4 W/m^2°C.

3. The temperature rise of each component in CPMSM is influenced by the ambient temperature. When the ambient temperature changes from –30°C to 30°C, the temperature rise of the winding decreased by 4.14%, the temperature rise of the permanent magnets decreased by 3.62%, the temperature rise of the can sleeve decreased by 3.47%, and the temperature rise of the winding insulation decreased by 3.84%.

References

[1] Li D., He Z., Sun S., Xing Z., *Dynamic characteristics modelling and analysis for dry screw vacuum pumps*, Vacuum, vol. 198, 110868 (2022), DOI: 10.1016/j.vacuum.2022.110868.

[2] Tang M., Wang C., Luo Y., *Predictive current control for permanent magnet synchronous motor based on internal model control observer*, Archives of Electrical Engineering, vol. 71, no. 2, pp. 343–362 (2022), DOI: 10.24425/aee.2022.140715.

[3] Garg V.K., Raymond J., *Magneto-thermal coupled analysis of canned induction motor*, IEEE Transactions on Energy conversion, vol. 5, no. 1, pp. 110–114 (1990), DOI: 10.1109/60.50821.

[4] Knypiński Ł., Krupiński J., *The slewing drive system for tower crane with permanent magnet synchronous motor*, Archives of Electrical Engineering, vol. 70, no. 1, pp. 189–201 (2021), DOI: 10.24425/aee.2021.136061.

[5] Wu Q., Li W., Li J. *et al.*, *Electromagnetic-thermal analysis of high-temperature direct drive electric-actuated valve canned permanent magnet synchronous motor*, IEEJ Transactions on Electrical and Electronic Engineering, vol. 18, no. 1, pp. 105–119 (2023), DOI: 10.1002/tee.23703.

[6] Li M., An Y., Zhang Z. *et al.*, *Effect of time harmonic current considering load condition on performance of canned induction motor*, International Journal of Applied Electromagnetics and Mechanics, vol. 66, no. 3, pp. 369–385 (2021), DOI: 10.3233/JAE-201552.

[7] Zhao H., Eldeeb H.H., Zhan Y. *et al.*, *Robust electromagnetic design of double-canned IM for submergible rim driven thrusters to reduce losses and vibration*, IEEE Transactions on Energy Conversion, vol. 35, no. 3, pp. 2045–2055 (2020), DOI: 10.1109/TEC.2020.3008415.

[8] Yu Q., Zhuang H., Tian L., *Modeling and thermal analysis of a canned permanent magnet machine with a novel network model*, International Journal of Applied Electromagnetics and Mechanics, vol. 65, no. 3, pp. 467–485 (2021), DOI: 10.3233/JAE-200020.

[9] Liang Y., Bian X., Yu H. *et al.*, *Finite-element evaluation and eddy-current loss decrease in stator end metallic parts of a large double-canned induction motor*, IEEE Transactions on Industrial Electronics, vol. 62, no. 11, pp. 6779–6785 (2015), DOI: 10.1109/TIE.2015.2438051.

[10] Yu Q., Wang X., Cheng Y., *Electromagnetic and thermal coupled analysis of can effect of a novel canned switched reluctance machine as a hydraulic pump drive*, International Journal of Applied Electromagnetics and Mechanics, vol. 54, no. 1, pp. 131–140 (2017), DOI: 10.3233/JAE-160126.

[11] Yu Q., Wang X., Cheng Y., *Thermal analysis of a canned switched reluctance drive with a novel network*, Applied Thermal Engineering, vol. 109, pp. 535–541 (2016), DOI: 10.1016/j.applthermaleng.2016.08.094.

[12] Tinni A., Knittel D., Nouari M. *et al.*, *Electrical–thermal modeling of a double-canned induction motor for electrical performance analysis and motor lifetime determination*, Electrical Engineering, vol. 103, pp. 103–114 (2021), DOI: 10.1007/s00202-020-01062-y.

[13] Yu Q., Li W., Chu S. *et al.*, *An optimal control scheme of canned switched reluctance motors for hydraulic pumps*, International Journal of Applied Electromagnetics and Mechanics, vol. 58, no. 1, pp. 1–13 (2018), DOI: 10.3233/JAE-180026.

[14] Ai L., Lu Y., Han J. *et al.*, *Simulation of the temperature of a shielding induction motor of the nuclear main pump under different turbulence models*, Energies, vol. 16, no. 6, pp. 2792–2801 (2023), DOI: 10.3390/en16062792.

[15] Li Y., Zhang C., Xu X., *Bidirectional electromagnetic–thermal coupling analysis for permanent magnet traction motors under complex operating conditions*, Transactions of the Canadian Society for Mechanical Engineering, vol. 46, no. 3, pp. 541–560 (2022), DOI: 10.1139/tcsme-2022-0010.

[16] Zwolnik T., Opach S., Cyganik Ł. *et al.*, *Design methods for limiting rotor losses in a fractional slot PMSM motor with high power density*, Archives of Electrical Engineering, vol. 71, no. 4, pp. 963–979 (2022), DOI: 10.24425/aee.2022.142119.

[17] Barański M., *Comparative analysis of the power parameters of a line start permanent magnet synchronous motor using professional FEM packages and in-house software*, Archives of Electrical Engineering, vol. 72, no. 3, pp. 585–596 (2023), DOI: 10.24425/aee.2023.146038.

[18] Soltani M., Nuzzo S., Barater D. *et al.*, *Investigation of the temperature effects on copper losses in hairpin windings*, Machines, vol. 10, no. 8, pp. 715–720 (2022), DOI: 10.3390/machines10080715.

[19] Okamoto S., Denis N., Kato Y. *et al.*, *Core loss reduction of an interior permanent-magnet synchronous motor using amorphous stator core*, IEEE Transactions on Industry Applications, vol. 52, no. 3, pp. 2261–2268 (2016), DOI: 10.1109/TIA.2016.2532279.

[20] Feng G., Lai C., Tjong J. *et al.*, *Noninvasive Kalman Filter Based Permanent Magnet Temperature Estimation for Permanent Magnet Synchronous Machines*, IEEE Transactions on Power Electronics, vol. 33, no. 12, pp. 10673–10682 (2018), DOI: 10.1109/TPEL.2018.2808323.

[21] Shi W., Zhou X., *Online estimation method for permanent magnet temperature of high-density permanent magnet synchronous motor*, IEEJ Transactions on Electrical and Electronic Engineering, vol. 15, no. 5, pp. 751–756 (2020), DOI: 10.1002/tee.23111.

[22] Aksöz S., Öztürk E., Maraşlı N., *The measurement of thermal conductivity variation with temperature for solid materials*, Measurement, vol. 46, no. 1, pp. 161–170 (2013), DOI: 10.1016/j.measurement.2012.06.003.

[23] Wei Y., Meng D., Wen J., *Heat exchange inside the motor*, China Machinery Industry Press (1998).

[24] Wang R., Fan X., Li D. *et al.*, *Comparison of heat transfer characteristics of the hollow-shaft oil cooling system for high-speed permanent magnet synchronous machines*, IEEE Transactions on Industry Applications, vol. 58, no. 5, pp. 6081–6092 (2022), DOI: 10.1109/TIA.2022.3182312.